

# Photochemical & Photobiological Sciences

Accepted Manuscript



This is an *Accepted Manuscript*, which has been through the Royal Society of Chemistry peer review process and has been accepted for publication.

*Accepted Manuscripts* are published online shortly after acceptance, before technical editing, formatting and proof reading. Using this free service, authors can make their results available to the community, in citable form, before we publish the edited article. We will replace this *Accepted Manuscript* with the edited and formatted *Advance Article* as soon as it is available.

You can find more information about *Accepted Manuscripts* in the [Information for Authors](#).

Please note that technical editing may introduce minor changes to the text and/or graphics, which may alter content. The journal's standard [Terms & Conditions](#) and the [Ethical guidelines](#) still apply. In no event shall the Royal Society of Chemistry be held responsible for any errors or omissions in this *Accepted Manuscript* or any consequences arising from the use of any information it contains.

## Enhanced sunlight photocatalytic activity of $\text{Ag}_3\text{PO}_4$ decorated novel combustion synthesis derived $\text{TiO}_2$ nanobelts for dye and bacterial degradation

Neerugatti KrishnaRao Eswar<sup>a</sup>, Praveen Chandrashekarapura Ramamurthy<sup>a,b</sup> and Giridhar Madras<sup>c\*</sup>

<sup>a</sup>Centre for Nanoscience and Engineering, <sup>b</sup>Department of Materials Engineering,

<sup>c</sup>Department of Chemical Engineering, Indian Institute of Science, Bangalore-560012

### ABSTRACT

This study demonstrates the synthesis of  $\text{TiO}_2$  nanobelts using solution combustion derived  $\text{TiO}_2$  with enhanced photocatalytic activity for dye degradation and bacterial inactivation. Hydrothermal treatment of combustion synthesized  $\text{TiO}_2$  resulted in unique partially etched  $\text{TiO}_2$  nanobelts and  $\text{Ag}_3\text{PO}_4$  was decorated using co-precipitation method. The catalyst particles were characterized using X-ray diffraction analysis, BET surface area analysis, diffused reflectance and electron microscopy. The photocatalytic properties of the composites of  $\text{Ag}_3\text{PO}_4$  with pristine combustion synthesized  $\text{TiO}_2$  and commercial  $\text{TiO}_2$  under sunlight were compared. Therefore the studies conducted proved that the novel  $\text{Ag}_3\text{PO}_4$ /unique combustion synthesis derived  $\text{TiO}_2$  nanobelts composite exhibited extended light absorption, better charge transfer mechanism and higher generation of hydroxyl and hole radicals. These properties resulted in enhanced photodegradation of dyes and bacteria when compared to commercial  $\text{TiO}_2$  nanocomposite. These findings have important implications in designing new photocatalysts for water purification.

**KEYWORDS:** *Solution combustion; nanobelts; solar radiation; dye degradation; bacterial inactivation.*

\*Corresponding author. Tel. +91 80 22932321; Fax: +91 80 23600683,

E-mail: [giridhar@chemeng.iisc.ernet.in](mailto:giridhar@chemeng.iisc.ernet.in) (G. Madras)

## 1. Introduction

As a result of radical urbanization, the quality of water has been compromised. Further, improper waste water treatment in industries, dumping of wastes causes water pollution. Besides chemical contamination, bacterial infections pertaining to water contamination must also be considered seriously. Fecal bacteria such as *Escherichia*, *fecal coliforms*, *Staphylococcus*, *Pseudomonas*, *Streptococcus* species in water cause various infections<sup>1</sup> and are a menace to public health.<sup>2</sup> The primary objective of any disinfection process in water treatment is the control of water-borne diseases through inactivation of pathogenic microorganisms in the water.<sup>3</sup>

Generation of reactive oxygen species to degrade the chemical contaminants and pathogens by advanced oxidation process using nanoparticles is one of the solutions for water purification. Over the past years, research on nanomaterials is increasing rapidly because of their valuable properties. There are several methods of synthesis of nanomaterials and varying morphologies such as nanorods, spheres, discs, nanoflowers, platelets etc.<sup>4, 5</sup> have been obtained and used for different applications like photocatalysis, electrocatalysis, supercapacitors etc.<sup>6, 7</sup>

Metal oxides such as ZnO, TiO<sub>2</sub> etc. and metals like Ag and Au have been used for various catalytic applications.<sup>8, 9</sup> Among various routes such as sol-gel, hydrothermal, solvothermal, aerosol, inert gas condensation, combustion synthesis of nanomaterials is considered to be quick and efficient. Combustion synthesized TiO<sub>2</sub> has proved to be an efficient catalyst compared to its commercial counterpart<sup>10, 11</sup>. However, many studies have attempted to increase the photoactivity of TiO<sub>2</sub>, since its efficiency depends on parameters such as particle size, crystallinity and pore size<sup>12</sup> etc. Efforts have been made to increase the photoactivity by doping with various transition elements.<sup>13</sup>

Silver and silver based compounds such as AgBr, AgI, Ag<sub>3</sub>PO<sub>4</sub>, have been used for photocatalytic and antibacterial applications.<sup>14-16</sup> Silver is being used as an effective antimicrobial agent because silver exhibits strong cytotoxic activity against a broad range of microbial organisms.<sup>17</sup> Recently, in addition to pristine silver, silver based photocatalysts are used widely for photocatalytic applications. AgBr on AgVO<sub>3</sub> nanobelts has shown efficient plasmonic photocatalytic activity against Rhodamine-B with good stability.<sup>16</sup> Surfactant assisted high-crystalline AgI nano plates showed better photocatalytic activity under visible light.<sup>14</sup> Ag<sub>3</sub>PO<sub>4</sub>, Ag/Ag<sub>3</sub>PO<sub>4</sub> showed better absorption of visible light and exhibits excellent antibacterial activity.<sup>18</sup> Recent studies on the activity of AgBr composite with iron oxide has enhanced the photocatalytic activity under visible light<sup>19, 20</sup>. Similarly Ag<sub>3</sub>PO<sub>4</sub> composite with TiO<sub>2</sub> Fe<sub>2</sub>O<sub>3</sub> and GO has shown better and synergistic photocatalytic activity compared to their pristine composition and also by facilitating magnetic separation of the photocatalyst<sup>21-24</sup>.

In this study, TiO<sub>2</sub> (CST) was prepared by the solution combustion method using ascorbic acid as a reducer. Recent reports have shown that as the nature of the TiO<sub>2</sub> precursors varies, the attributes of the nanobelts derived from them changes significantly<sup>25</sup>. The TiO<sub>2</sub> nanobelts (CSTNB) were synthesized using combustion synthesized TiO<sub>2</sub> as a novel precursor. Ag<sub>3</sub>PO<sub>4</sub> has been impregnated on these TiO<sub>2</sub> nanobelts by simple co-precipitation technique. This is the first study to report impregnation of Ag<sub>3</sub>PO<sub>4</sub> on TiO<sub>2</sub> nanobelts prepared using combustion synthesized TiO<sub>2</sub> as a precursor for photocatalysis under natural sunlight. The photocatalytic degradation of organic pollutants and antibacterial activity of Ag<sub>3</sub>PO<sub>4</sub> impregnated combustion synthesized TiO<sub>2</sub> and TiO<sub>2</sub> nanobelt compounds has been compared with commercial TiO<sub>2</sub> (Degussa P-25).

## 2. Experimental

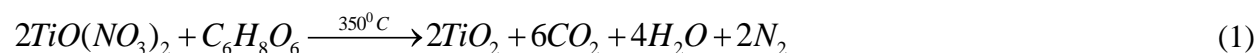
### 2.1. Materials

Titanium iso-propoxide (>97% purity) was purchased from Sigma-Aldrich. L-ascorbic acid-LR, silver nitrate, di-sodium hydrogen phosphate and methylene blue, methyl orange, neutral red dyes were purchased from SD Fine chemicals Ltd. (India). Sodium hydroxide, sulphuric acid (98%), hydrochloric acid (35%) and nitric acid (69%) were purchased from Merck (India). Neubauer-chamber was purchased from Pristine Scientific Ltd. (India). Luria nutrient broth was purchased from Hi Media (India). Double distilled Millipore water was used for all the experiments.

### 2.2. Catalyst Preparation

#### 2.2.1. Synthesis of TiO<sub>2</sub> using solution combustion method

TiO<sub>2</sub> nanoparticles were prepared using solution combustion method<sup>10</sup> with ascorbic acid as reducer and titanyl nitrate as oxidizer. A typical synthesis of titanyl nitrate involves mixing titanium iso-propoxide in ice-cold water to obtain a white precipitate. To the above precipitate, 1:2 nitric acid (by volume) was added to obtain a transparent solution of titanyl nitrate. Equimolar oxidizer to fuel ratio was maintained by adding titanyl nitrate with stoichiometric amount of L-ascorbic acid. The combustion reaction is,



The reaction mixture was kept in a preheated furnace at 350°C for 15 min and a smoldering combustion reaction was observed. The combustion product was grounded finely to obtain a pale yellow colored powder.

### 2.2.2. Synthesis of TiO<sub>2</sub> nanobelts from combustion synthesized TiO<sub>2</sub>

TiO<sub>2</sub> nanobelts (CSTNB) was prepared from combustion synthesized TiO<sub>2</sub>.<sup>26</sup> 20 ml of 10 M sodium hydroxide was mixed with 0.1 g of combustion synthesized TiO<sub>2</sub> and stirred vigorously. Later the mixture was transferred into Teflon coated steel autoclave and kept inside the furnace at 180°C for 48 h. The nature of nanobelt remains the same by varying the temperature of hydrothermal reaction from 180°C to 240°C<sup>27, 28</sup>. Hence, the optimum temperature is considered as 180°C and 48 h. Similarly, after hydrothermal treatment of TiO<sub>2</sub> with NaOH, Na<sub>2</sub>Ti<sub>3</sub>O<sub>7</sub> is formed. The obtained powder was washed with de-ionized water several times to remove impurities and then dispersed in 0.1 M HCl. Treating this product with HCl involves ion exchange to become H<sub>2</sub>Ti<sub>3</sub>O<sub>7</sub>. In order to remove the impurities, the product formed was thoroughly washed with de-ionized water until the pH of the washed solution becomes 7. Later H<sub>2</sub>Ti<sub>3</sub>O<sub>7</sub> belts were dispersed in 40 ml of 0.02 M sulphuric acid and transferred to Teflon coated steel autoclave. The autoclave was maintained at 100°C for 12 h to obtain acid etched H<sub>2</sub>Ti<sub>3</sub>O<sub>7</sub> belts. However, increase in concentration or reaction time during acid corrosion of combustion synthesis derived TiO<sub>2</sub> nanobelts changes the structure of belt by disintegrating them into fine nanoparticles. Hence, 0.02 M of H<sub>2</sub>SO<sub>4</sub> and 12 h reaction at 100°C considered as optimal. The resultant product was centrifuged at 5000 rpm for 10 min and washed several times with de-ionized water, later dried at 70°C for 10 h. The dried powder was annealed at 600°C for 2 h to obtain white colored acid etched TiO<sub>2</sub> nanobelts (CSTNB).

### 2.2.3. Synthesis of Ag<sub>3</sub>PO<sub>4</sub>, Ag<sub>3</sub>PO<sub>4</sub>/CST and Ag<sub>3</sub>PO<sub>4</sub>/CSTNB

A simple co-precipitation technique was used to prepare Ag<sub>3</sub>PO<sub>4</sub>/CST and Ag<sub>3</sub>PO<sub>4</sub>/CSTNB heterostructures. Initially, 0.2 g acid-etched TiO<sub>2</sub> nanobelts (CSTNB) were dispersed in 100 ml of de-ionized water in a separate round bottom flask. The mixture was ultrasonicated for 15 min. Stoichiometric amount of silver nitrate and di-sodium hydrogen phosphate solution was prepared

separately using de-ionized water. Silver nitrate solution (1:10 of  $\text{Ag}_3\text{PO}_4:\text{TiO}_2$ ) was added drop wise to the  $\text{TiO}_2$  nanobelt dispersed mixture while continuing with vigorous stirring at  $60^\circ\text{C}$ . The pH of the mixture was kept at 5 using 0.1 M nitric acid.

For comparison, the same process was carried out for the preparation of  $\text{Ag}_3\text{PO}_4/\text{CST}$  and  $\text{Ag}_3\text{PO}_4/\text{P-25}$  using combustion synthesized  $\text{TiO}_2$  and commercial Degussa P-25 instead of  $\text{TiO}_2$  nanobelts. Disodium hydrogen phosphate solution was added slowly into the above mixture until the solution turns pale yellow indicating formation of  $\text{Ag}_3\text{PO}_4$  on CST and CSTNB. Pristine  $\text{Ag}_3\text{PO}_4$  was prepared by the same procedure but without the addition of  $\text{TiO}_2$  nanoparticles.

### 3. Characterization

X-ray diffraction spectra were obtained from Rigaku diffractometer using  $\text{Cu-K}\alpha$  radiation with a scan rate of  $1^\circ/\text{min}$  in the scan range of  $10^\circ$ - $80^\circ$ . Scanning electron micrographs were captured using ULTRA55 FESEM, Carl Zeiss. The samples were dispersed in absolute ethanol and sonicated for 10 min. These dispersed samples were drop-casted on silica wafers which were stuck to carbon tape on SEM aluminium stub. The prepared samples were kept under vacuum for 12 h; after that samples were gold sputtered using Quaram sputtering machine to prevent sample charging effect and SEM images were taken. Transmission electron micrographs were acquired with Tecnai T20 operated at 180 kV. Samples for TEM analysis were prepared by dispersing it in isopropanol and subjected to ultrasonication. Later, the samples were drop casted on copper grid and kept under vacuum for 12 h. Diffused reflectance spectra were obtained using solid state UV-visible spectrophotometer (Perkin Elmer). Photoluminescence measurements were performed using PL-Spectrophotometer (Perkin Elmer). The absorbance measurements for photocatalysis experiments were measured using UV-Visible spectrophotometer (Shimadzu-UV 1700). Samples were regenerated at  $120^\circ\text{C}$  for 2 h prior for

BET surface analysis using Nova-1000 Quantachrome. The data was obtained by using Belsorb surface area analyzer (Smart instruments) with the help of liquid nitrogen (77 K) and water (300 K) atmospheres for both adsorption and desorption of N<sub>2</sub>.

#### **4. Photochemical reactor and photocatalysis**

100 ml quartz reactors were used to perform photocatalytic experiments. Photocatalytic dye degradation and antibacterial degradation experiments were conducted under direct sunlight between 11:00 am to 2:00 pm, when the solar intensity fluctuations are less and the intensity was  $\sim 975 \text{ W/m}^2$ . The reaction mixture was stirred vigorously using a magnetic stirrer and the samples were collected from the reactor at specific time to measure absorbance. Experiments were done in dark to measure the adsorption of dye over catalyst particles.

Photocatalysis was performed using 20 ppm aqueous solution of methylene blue and 30 ppm aqueous solution of methyl orange. The catalyst concentration was maintained as 1 g/l for all the experiments. The catalyst particles were initially suspended in the dye solution and kept in dark for 1 h to achieve stable absorption-desorption equilibrium. Samples were collected from the reactor at regular intervals and centrifuged at 5000 rpm for 5 min to separate catalyst particles from solution and absorbance was measured using UV-visible spectrophotometer.

##### **4.1. Antibacterial evaluation**

Bacterial culture of wild type *Escherichia coli* strain was prepared using liquid nutrient broth. Glass wares, media, test tubes, Eppendorf tubes, micro tips etc. and all other accessories required for culture preparation and antibacterial evaluation were autoclaved and kept under UV light inside a laminar chamber. Bacterial culture was centrifuged at 5000 rpm for 10 minutes to separate bacterial cells as pellet. Later, the pellet was re-suspended in phosphate buffer saline solution in order to maintain the



ionic concentration for the bacteria. Control experiments were conducted in dark using 0.25 g/l catalyst and bacterial suspension alone without keeping the reactor under solar irradiation. Further, the catalysts were added into fresh bacterial suspension and kept under solar radiation. Sample mixtures of bacterial and catalyst suspensions were collected at regular intervals in order to measure antibacterial activity. Various methods such as broth dilution, turbidity assay, colony-counting, disk-diffusion, growth inhibition, minimum inhibitory concentration. In addition to that, Neubauer-chamber counting etc. can be used for the quantitative or qualitative determination of anti-microbial activity.<sup>29, 30</sup> 100  $\mu$ l of serially diluted aliquots were mixed with 0.4% of neutral red solution according to 1:10 ratio. 20  $\mu$ l of the above stained bacterial suspension was pipetted out on Neubauer counting chamber. The viable bacterial cells were stained by neutral red because live cells incorporate the stain into lysosomes. Live bacterial cells were counted on respective squares under microscope and averaged for calculating bacterial cell density.

## 5. Results and discussions

### 5.1. X-ray diffraction analysis

X-ray diffraction patterns of combustion synthesized TiO<sub>2</sub> and acid etched TiO<sub>2</sub> nanobelts were shown in Fig.1 (a) and Fig.1 (b). The synthesized product with ascorbic acid as fuel for combustion has shown the possibility of formation of rutile phase at  $2\theta$  value of 36.0° and 54.2° (JCPDS No: 00-001-1292) besides a predominant anatase phase. The anatase can be observed at  $2\theta$  value of 25.4° (JCPDS No: 00-004-0477) with (101) as  $\langle hkl \rangle$  parameters. It has been reported that combustion synthesis of TiO<sub>2</sub> using titanyl nitrate and ascorbic acid of 5:3 molar ratio between oxidizer and fuel resulted in pure anatase phase.<sup>31</sup> However, if the stoichiometric ratio is 2:1, rutile phase is formed which co-exists with anatase.

The X-ray diffraction pattern of nanobelts prepared out of combustion synthesized  $\text{TiO}_2$  shows a huge peak that corresponds to the anatase phase (JCPDS No: 00-004-0477) and adjacent to it a small peak at  $27.6^\circ$  corresponding to the rutile phase (JCPDS No: 00-001-1292). The diffraction peaks for  $\text{Ag}_3\text{PO}_4$  nanoparticles are denoted with filled dots (Fig.1(c)) and at  $33.4^\circ$  a huge peak was observed which corresponds to (210) plane diffraction. Further peaks at  $36.7^\circ$ ,  $55.0^\circ$ ,  $57.5^\circ$ , and  $61.9^\circ$ , can be assigned to the diffractions from the (2 1 0), (3 1 0), (3 2 0), (3 2 1), and (4 0 0) planes of  $\text{Ag}_3\text{PO}_4$  (JCPDS (00-006-0505)). This pattern was also manifested in the  $\text{Ag}_3\text{PO}_4/\text{TiO}_2$  nano heterostructures (Fig.1 (d)). Therefore, successful impregnation of  $\text{Ag}_3\text{PO}_4$  over acid etched  $\text{TiO}_2$  nanobelts can be corroborated based on these observations.

## 5.2. Diffuse reflectance spectrophotometry

The UV-vis diffuse reflectance spectra of the  $\text{Ag}_3\text{PO}_4$ , acid etched  $\text{TiO}_2$  nanobelts and  $\text{Ag}_3\text{PO}_4$  coupled acid etched  $\text{TiO}_2$  nanobelts were measured using UV-Vis spectrophotometer (Perkin Elmer). The formation of  $\text{Ag}_3\text{PO}_4/\text{TiO}_2$  has accounted to a remarkable increase in light absorption in the visible region compared to pristine  $\text{TiO}_2$  nanobelts. As shown in Fig.2, UV-vis diffuse reflectance spectroscopic measurements rendered that the acid-etched  $\text{TiO}_2$  nanobelts exhibited a strong absorption at about 390 nm, which can be corresponded to the band gap of multi-phase titania having both anatase and rutile (3.0-3.2 eV).<sup>32</sup> Similarly, a strong absorption peak was recorded at around 550 nm which can be matched to  $\text{Ag}_3\text{PO}_4$  nanoparticles whose in-direct band gap was calculated as around 2.4 eV.<sup>33</sup> The absorption edge of the  $\text{Ag}_3\text{PO}_4$  impregnated  $\text{TiO}_2$  heterostructures was unaltered compared to the pristine acid etched  $\text{TiO}_2$  nanobelts. However, there was a strong absorbance in the visible region between 400 and 700 nm. This can confirm that  $\text{Ag}_3\text{PO}_4$  was successfully impregnated over the acid etched  $\text{TiO}_2$  nanobelts.<sup>33, 34</sup>

### 5.3. Microscopic analysis

The morphological features of acid etched TiO<sub>2</sub> nanobelts and Ag<sub>3</sub>PO<sub>4</sub> impregnated TiO<sub>2</sub> nanobelts were studied using SEM and HRTEM micrographs. SEM image of acid etched TiO<sub>2</sub> nanobelts before acid treatment was shown in Fig. 3 (a). An acid corrosion treatment led to partial etching of nanobelts and subsequent formation of several TiO<sub>2</sub> islands on existing nanobelts and also on partially etched nanobelts, as shown in Fig.3 (b). The surface area of TiO<sub>2</sub> nanobelts was 35 m<sup>2</sup>/g and it has increased to 75 m<sup>2</sup>/g after acid etching process.<sup>35</sup> It can be suggested that etched surfaces could serve as nucleating site for Ag<sub>3</sub>PO<sub>4</sub> nanoparticles, resulting in the formation of Ag<sub>3</sub>PO<sub>4</sub>/TiO<sub>2</sub> composite, as shown in (Fig.3 (c)). One can observe that the Ag<sub>3</sub>PO<sub>4</sub> nanoparticles, with an approximate diameter between 10 and 20 nm, were deposited onto the acid-etched TiO<sub>2</sub>nanobelts surface, consistent with TEM image Fig.3 (e). Ag<sub>3</sub>PO<sub>4</sub> nanoparticles were also prepared without the acid etched TiO<sub>2</sub> nanobelt support, following similar experimental conditions excluding the addition of TiO<sub>2</sub> nanobelts. Ag<sub>3</sub>PO<sub>4</sub> nanoparticles were spherical shape mostly agglomerated with other particles, as shown in Fig.3 (d). The structural analysis of the Ag<sub>3</sub>PO<sub>4</sub>/TiO<sub>2</sub> heterostructures was done by HRTEM.

As shown in Fig.3 (f), the lattice of both Ag<sub>3</sub>PO<sub>4</sub> and TiO<sub>2</sub> can be clearly distinguished. Ag<sub>3</sub>PO<sub>4</sub> particles have d-spacing of 0.56 nm, matching with the structure of Ag<sub>3</sub>PO<sub>4</sub>, whereas d-spacing of 0.35 nm was observed for the TiO<sub>2</sub> nanobelts, which corresponds to anatase TiO<sub>2</sub>. It can be clearly observed that the Ag<sub>3</sub>PO<sub>4</sub> was impregnated firmly to the TiO<sub>2</sub> nanobelt substrate, which promotes synergistic effect towards photocatalysis by promoting a wide optical absorption and also ensures structural stability of the composite.

#### 5.4. X-ray photoelectron spectroscopy

XPS results of silver in  $\text{Ag}_3\text{PO}_4/\text{CSTNB}$  show the existence of Ag in two bands corresponding to 368.2 and 374.1 eV respectively, ascribed to Ag  $3d_{5/2}$  and Ag  $3d_{3/2}$  (Fig. 4(a)). These bands correspond to the  $\text{Ag}^+$  of  $\text{Ag}_3\text{PO}_4$ . The band observed in Fig.4 (b) at 369.2 and 374.9 eV exhibit the binding energy of silver in  $\text{Ag}^0$  state. This proves that after exposing  $\text{Ag}_3\text{PO}_4$  (either in pristine or composite form) to light, part of  $\text{Ag}^+$  becomes  $\text{Ag}^0$ . In the case of just  $\text{Ag}_3\text{PO}_4$ , the  $\text{Ag}^0$  formation is very high and hence stability is low. However, when  $\text{Ag}_3\text{PO}_4$  is in composite form, there will be a formation of  $\text{Ag}/\text{Ag}_3\text{PO}_4/\text{substrate}$ <sup>36</sup> and hence prolonged activity of  $\text{Ag}_3\text{PO}_4$  is maintained.

#### 5.5. Photoluminescence spectroscopy

The photoluminescence spectra of  $\text{Ag}_3\text{PO}_4$  impregnated combustion synthesized  $\text{TiO}_2$  and acid etched  $\text{TiO}_2$  nanobelts are shown in fig.5. The presence of intrinsic states instead of surface states can be corroborated to the peak originating at 419 nm because of charge transfer transitions between the 2p orbitals of oxygen and empty d orbital of silver ion which could possibly lead to recombination during photoluminescence.<sup>37</sup> Recombination of self-trapped excitons in  $\text{PO}_4$  anionic complex could also be the reason of the emission peak at 419 nm. Peak at 533 nm which is approximately equal to band gap of  $\text{Ag}_3\text{PO}_4$  can be matched to the recombination of electrons at conduction band and holes at valence band edges.<sup>38, 39</sup> Surface deposited silver or Ag doped into  $\text{TiO}_2$  lattice can act as efficient traps for the photo-induced electrons that prevents recombination. However, if the presence of excess  $\text{Ag}^0$  could lead to reduction in the traps and increase in photoluminescence intensity as observed at 441 nm and 485 nm. Peak at 530 nm can also correspond to charge transfer between oxygen vacancies and  $\text{Ti}^{4+}$  including the peak at 460 nm which acts as traps for charge.<sup>40</sup> In the case of  $\text{Ag}_3\text{PO}_4$  impregnated with acid etched  $\text{TiO}_2$  nanobelts the photoluminescence intensity decreased significantly which can be attributed due to efficient charge transfer and charge separation mechanism.

## 5.6. Photocatalysis

### 5.6.1. Photocatalytic degradation of dyes

The photocatalytic performance of  $\text{Ag}_3\text{PO}_4/\text{CST}$  and  $\text{Ag}_3\text{PO}_4/\text{CSTNB}$  was assessed by the degradation of organic dye molecules under sunlight irradiation. Fig. 6 (a) and 6 (b) shows the degradation of both cationic (methylene blue) and anionic (methyl orange) dyes. These catalysts were compared to the composite of  $\text{Ag}_3\text{PO}_4$  with standard commercial grade  $\text{TiO}_2$ , Degussa P-25 ( $\text{Ag}_3\text{PO}_4/\text{P-25}$ ). Photodegradation experiments were also conducted using pristine  $\text{Ag}_3\text{PO}_4$ . The blank experiments were conducted in the absence of sunlight, where the catalysts were experimented for adsorption. All the catalysts showed adsorption around 15% of initial dye concentration. Pristine  $\text{Ag}_3\text{PO}_4$  showed negligible adsorption over both the dyes. The photocatalytic efficiency of  $\text{Ag}_3\text{PO}_4/\text{CSTNB}$  was significantly higher compared to other composites. Though the photocatalytic activity of  $\text{Ag}_3\text{PO}_4$  was higher compared to the composites, the stability of  $\text{Ag}_3\text{PO}_4$  reduced over subsequent runs<sup>34</sup>.  $\text{Ag}_3\text{PO}_4/\text{TiO}_2$  nanobelts showed very high photocatalytic activity for all the dyes. This is due to efficient charge separation that could happen in the  $\text{TiO}_2$  nanobelts and also potential charge transfer at the interface of acid etched  $\text{TiO}_2$  nanobelts and  $\text{Ag}_3\text{PO}_4$ . Both the cationic and anionic dyes degraded 100% within 20 and 30 min, respectively, under solar irradiation with  $\text{Ag}_3\text{PO}_4/\text{CSTNB}$ . However, in the presence of  $\text{Ag}_3\text{PO}_4/\text{CST}$  and  $\text{Ag}_3\text{PO}_4/\text{P-25}$ , it took 30 and 40 min respectively for the dyes to degrade completely. The degradation was analyzed by plotting  $C/C_0$  with time.  $\ln(C/C_0) = kt$  is the first order kinetic equation that corresponds to the photocatalytic degradation, where  $C_0$  is the initial concentration,  $C$  is the final concentration of the reactant at time  $t$  and  $k$  is the apparent rate constant. The slope of the linear plot of  $\ln(C/C_0)$  versus time gives the apparent rate constant  $k$ . The apparent rate constants of all the catalysts are tabulated (Table 1). From the kinetic plot, as shown in Fig.6 (c) and Fig.6 (d), the rate constant obtained for  $\text{Ag}_3\text{PO}_4/\text{CSTNB}$  for both methylene blue and methyl

orange degradation was very high compared to  $\text{Ag}_3\text{PO}_4/\text{CST}$  and  $\text{Ag}_3\text{PO}_4/\text{P-25}$  indicating its superior photocatalytic activity. The efficient charge separation because of island – belt interactions, majority of active phase exposure, and wide range of optical absorption of light by the composite could be possible reasons for the enhanced photoactivity exhibited by  $\text{Ag}_3\text{PO}_4$  coupled acid etched  $\text{TiO}_2$  nanobelts.

### 5.6.2. Antimicrobial activity

The bacterial degradation experiments were performed under natural sunlight using  $\text{Ag}_3\text{PO}_4/\text{P-25}$ ,  $\text{Ag}_3\text{PO}_4/\text{CST}$ ,  $\text{Ag}_3\text{PO}_4/\text{CSTNB}$  and  $\text{Ag}_3\text{PO}_4$ . Photolysis experiments were done without any catalyst particles in the bacterial suspension. Control experiments were also carried on using just the catalysts in the bacterial suspension but in the absence of sunlight. As shown in Fig.7 (a). From Fig.7 (b), it is evident that  $\text{Ag}_3\text{PO}_4/\text{CSTNB}$  was efficient for the inactivation of the microorganisms compared to other composites. Pristine  $\text{Ag}_3\text{PO}_4$  shows high antimicrobial activity against *E.coli*.  $\text{Ag}_3\text{PO}_4$  can also slowly release Ag ions into the solution. Therefore, the composites have shown significant bacterial reduction compared to its  $\text{TiO}_2$  counterpart in the composite. Upon exposure to sunlight,  $\text{Ag}_3\text{PO}_4$  turned dark within a short period of time unlike the composites, indicating that part of  $\text{Ag}^+$  was reduced to  $\text{Ag}^0$ . The reactive radical species generated by the catalyst was responsible for the killing of bacteria. The generated radicals would break the polyunsaturated phospholipid structures that are present in *E.coli*, which ruptures cell membrane leading to bacterial degradation<sup>41, 42</sup> and also damaging the nucleic matter of bacteria.<sup>43, 44</sup> Therefore,  $\text{Ag}_3\text{PO}_4$  coupled with acid-etched  $\text{TiO}_2$  nanobelt structures exhibits superior antibacterial activity by generating more hydroxyl radicals combined with synergistic effect of Ag.<sup>45</sup> In the dark experiments, antibacterial activity of  $\text{Ag}_3\text{PO}_4$  and composites is due to release of  $\text{Ag}^+$  ions. Silver ions and silver nanoparticles are efficient bactericidal agents<sup>46</sup>. Therefore, upon irradiating sunlight,  $\text{Ag}_3\text{PO}_4$  acts as an efficient semiconductor, where charge carriers take part in photocatalytic degradation of dyes and bacteria. When  $\text{Ag}_3\text{PO}_4$  coupled with  $\text{TiO}_2$

nanobelts, the photoactivity is still enhanced by extending the light absorption towards visible region by the photocatalyst, maintaining stability of the photocatalyst by reducing the release of  $\text{Ag}^+$  ions into solution<sup>45, 47, 48</sup>.

At dark conditions with  $\text{Ag}_3\text{PO}_4$  in a bacterial suspension, bactericidal effect was observed because of release of  $\text{Ag}^+$  ions into the suspension<sup>47</sup>. However, this process occurs at times scales greater than 2 h. Thus the release of Ag does not influence photocatalytic activity for the degradation of dyes but has some activity towards the inactivation of bacteria. Therefore, it is considered best to employ  $\text{Ag}_3\text{PO}_4$  as a photocatalyst and investigate the bactericidal effect under UV/solar light. Similarly, using pristine  $\text{Ag}_3\text{PO}_4$  for methylene blue degradation showed best activity during initially but the photoactivity of  $\text{Ag}_3\text{PO}_4$  decreased over subsequent trials, as discussed in the later section on reusability. This was observed by decrease in photocatalytic activity and also by observing change in color of  $\text{Ag}_3\text{PO}_4$  from yellow to black because of formation of Ag nanoparticles upon shining light. But this was not observed when  $\text{Ag}_3\text{PO}_4$  was impregnated with nanobelt structures, where the latter acts as the support preventing decrease in photoactivity of  $\text{Ag}_3\text{PO}_4$ . Thus  $\text{Ag}_3\text{PO}_4$  decorated  $\text{TiO}_2$  nanobelts are the best for photocatalytic degradation for dyes and bacteria.

### 5.7. Scavenger reactions

It is known that principal factor of photocatalysis is generation of reactive radicals. Therefore, it is necessary to evaluate the nature of the reactive radicals responsible for the catalytic degradation. The photocatalytic reactant mixture was mixed with various scavengers and the degradation was carried out. EDTA- $2\text{Na}^+$  (hole scavenger),<sup>49</sup> tertiary-butyl alcohol ( $\bullet\text{OH}$  scavenger),<sup>50</sup> DMSO ( $e^-$  scavenger),<sup>51</sup> benzoquinone ( $\text{O}_2^{\bullet-}$  scavenger)<sup>52</sup> were the scavengers added to the reaction mixture containing

methylene blue and catalyst particles and subjected to photocatalytic degradation under sunlight. From fig.8, it is observed that photocatalytic generated holes and hydroxyl radicals formed during the reaction by the  $\text{Ag}_3\text{PO}_4$  and acid etched  $\text{TiO}_2$  nanobelts composite are responsible for the efficient degradation. There is a huge probability for the holes generated from  $\text{TiO}_2$  excitation to get transported towards  $\text{Ag}_3\text{PO}_4$ , and thus the generation of hydroxyl radical is highly favorable. The excited electrons of  $\text{Ag}_3\text{PO}_4$ , in addition to transported electrons from anatase, also take part in generation of  $\text{O}_2^{*-}$  radicals.

### 5.8. Stability

The reusability of the catalyst has been performed by photo-degrading methylene blue under solar radiation. The catalyst particles were centrifuged and dried at  $100^\circ\text{C}$  after each cycle. The catalytic stability was shown in fig.9 as a 3D profile representing methylene blue degradation with respect to each cycle. As compared to the pristine  $\text{Ag}_3\text{PO}_4$ ,  $\text{Ag}_3\text{PO}_4$  impregnated on acid-etched  $\text{TiO}_2$  nanobelts shows consistent photocatalytic activity even after 3 cycles. This might be due to tight anchoring of  $\text{Ag}_3\text{PO}_4$  on the surface of acid etched nanobelts that enhances the stability of the composites.

### 6. Conclusions

This study indicates the outstanding properties exhibited by the novel combustion synthesis derived  $\text{TiO}_2$  nanobelts compared to commercial  $\text{TiO}_2$ .  $\text{TiO}_2$  nanobelts were synthesized using combustion synthesized  $\text{TiO}_2$  for the first time. The synthesis and photodegradation experiments of composite  $\text{Ag}_3\text{PO}_4$  coupled with acid etched combustion synthesized  $\text{TiO}_2$  nanobelts were performed. The photocatalytic activity of  $\text{Ag}_3\text{PO}_4/\text{CSTNB}$  composite was significantly higher compared to  $\text{Ag}_3\text{PO}_4/\text{CST}$  and  $\text{Ag}_3\text{PO}_4/\text{P-25}$ . The efficient and excess generation of hydroxyl radicals by the  $\text{Ag}_3\text{PO}_4/\text{CSTNB}$  due to lower recombination and better charge transfer led to enhanced photoactivity.



TiO<sub>2</sub> islands and Ag<sub>3</sub>PO<sub>4</sub> impregnation on top of acid etched TiO<sub>2</sub> nanobelts has not only contributed towards enhanced charge separation but also efficient charge transfer and utilization of broad spectrum of light for a better photocatalytic activity for the degradation of dyes and inactivation of bacteria.

## 7. Acknowledgements

The authors are thankful to Department of Science and Technology, India for the financial support. The authors thank Prof. Jayant Modak, Department of Chemical Engineering, IISc, for extending facilities to perform antibacterial experiments.

## References

1. T. Schwartz, W. Kohlen, B. Jansen and U. Obst, Detection of antibiotic-resistant bacteria and their resistance genes in wastewater, surface water, and drinking water biofilms, *FEMS Microbiology Ecology*, 2003, **43**, 325-335.
2. D. D. Mara, S. Cairncross and W. H. Organization, Guidelines for the safe use of wastewater and excreta in agriculture and aquaculture: measures for public health protection/prepared by Duncan Mara & Sandy Cairncross, 1989.
3. M. D. Sobsey, Inactivation of health-related microorganisms in water by disinfection processes, *Water Science & Technology*, 1989, **21**, 179-195.
4. G. Korotcenkov, The role of morphology and crystallographic structure of metal oxides in response of conductometric-type gas sensors, *Materials Science and Engineering: R: Reports*, 2008, **61**, 1-39.
5. T. M. Shang, J. H. Sun, Q. F. Zhou and M. Y. Guan, Controlled synthesis of various morphologies of nanostructured zinc oxide: flower, nanoplate, and urchin, *Crystal Research and Technology*, 2007, **42**, 1002-1006.
6. K. M. Kim, K.-Y. Kang, S. Kim and Y.-G. Lee, Electrochemical properties of TiO<sub>2</sub> nanotube-Li<sub>4</sub>Ti<sub>5</sub>O<sub>12</sub> composite anodes for lithium-ion batteries, *Current Applied Physics*, 2012, **12**, 1199-1206.
7. X. Wu, W. Xing, L. Zhang, S. Zhuo, J. Zhou, G. Wang and S. Qiao, Nickel nanoparticles prepared by hydrazine hydrate reduction and their application in supercapacitor, *Powder Technology*, 2012, **224**, 162-167.
8. A. Leelavathi, G. Madras and N. Ravishankar, Origin of enhanced photocatalytic activity and photoconduction in high aspect ratio ZnO nanorods, *Physical Chemistry Chemical Physics*, 2013, **15**, 10795-10802.
9. V. Subramanian, E. Wolf and P. V. Kamat, Semiconductor-metal composite nanostructures. To what extent do metal nanoparticles improve the photocatalytic activity of TiO<sub>2</sub> films?, *The Journal of Physical Chemistry B*, 2001, **105**, 11439-11446.
10. K. Nagaveni, M. Hegde, N. Ravishankar, G. Subbanna and G. Madras, Synthesis and structure of nanocrystalline TiO<sub>2</sub> with lower band gap showing high photocatalytic activity, *Langmuir*, 2004, **20**, 2900-2907.

11. K. Patil, M. Hegde, T. Rattan and S. Aruna, Chemistry of nanocrystalline oxide materials- Combustion synthesis, properties and applications, 2008.
12. Z. Zhang, C.-C. Wang, R. Zakaria and J. Y. Ying, Role of particle size in nanocrystalline TiO<sub>2</sub>-based photocatalysts, *The Journal of Physical Chemistry B*, 1998, **102**, 10871-10878.
13. K. Nagaveni, M. Hegde and G. Madras, Structure and Photocatalytic Activity of Ti<sub>1-x</sub>M<sub>x</sub>O<sub>2±δ</sub> (M= W, V, Ce, Zr, Fe, and Cu) Synthesized by Solution Combustion Method, *The Journal of Physical Chemistry B*, 2004, **108**, 20204-20212.
14. W. Jiang, C. An, J. Liu, S. Wang, L. Zhao, W. Guo and J. Liu, Facile aqueous synthesis of β-AgI nanoplates as efficient visible-light-responsive photocatalyst, *Dalton Transactions*, 2014, **43**, 300-305.
15. M. Ge, N. Zhu, Y. Zhao, J. Li and L. Liu, Sunlight-assisted degradation of dye pollutants in Ag<sub>3</sub>PO<sub>4</sub> suspension, *Industrial & engineering chemistry research*, 2012, **51**, 5167-5173.
16. Y. Sang, L. Kuai, C. Chen, Z. Fang and B. Geng, Fabrication of a Visible-Light-Driven Plasmonic Photocatalyst of AgVO<sub>3</sub>@AgBr@Ag Nanobelt Heterostructures, *ACS applied materials & interfaces*, 2014, **6**, 5061-5068.
17. J. S. Kim, E. Kuk, K. N. Yu, J.-H. Kim, S. J. Park, H. J. Lee, S. H. Kim, Y. K. Park, Y. H. Park and C.-Y. Hwang, Antimicrobial effects of silver nanoparticles, *Nanomedicine: Nanotechnology, Biology and Medicine*, 2007, **3**, 95-101.
18. Y. Liu, L. Fang, H. Lu, L. Liu, H. Wang and C. Hu, Highly efficient and stable Ag/Ag<sub>3</sub>PO<sub>4</sub> plasmonic photocatalyst in visible light, *Catalysis Communications*, 2012, **17**, 200-204.
19. H. Zhao, L. Zhang, X. Gu, S. Li, B. Li, H. Wang, J. Yang and J. Liu, Fe<sub>2</sub>O<sub>3</sub>-AgBr nonwoven cloth with hierarchical nanostructures as efficient and easily recyclable macroscale photocatalysts, *RSC Advances*, 2015, **5**, 10951-10959.
20. H. Yu, L. Xu, P. Wang, X. Wang and J. Yu, Enhanced photoinduced stability and photocatalytic activity of AgBr photocatalyst by surface modification of Fe (III) cocatalyst, *Applied Catalysis B: Environmental*, 2014, **144**, 75-82.
21. X. Yang, J. Qin, Y. Jiang, K. Chen, X. Yan, D. Zhang, R. Li and H. Tang, Fabrication of P25/Ag<sub>3</sub>PO<sub>4</sub>/graphene oxide heterostructures for enhanced solar photocatalytic degradation of organic pollutants and bacteria, *Applied Catalysis B: Environmental*, 2015, **166**, 231-240.
22. J.-W. Xu, Z.-D. Gao, K. Han, Y. Liu and Y.-Y. Song, Synthesis of Magnetically Separable Ag<sub>3</sub>PO<sub>4</sub>/TiO<sub>2</sub>/Fe<sub>3</sub>O<sub>4</sub> Heterostructure with Enhanced Photocatalytic Performance under Visible

- Light for Photoinactivation of Bacteria, *ACS applied materials & interfaces*, 2014, **6**, 15122-15131.
23. X. Yang, H. Cui, Y. Li, J. Qin, R. Zhang and H. Tang, Fabrication of Ag<sub>3</sub>PO<sub>4</sub>-Graphene composites with highly efficient and stable visible light photocatalytic performance, *ACS Catalysis*, 2013, **3**, 363-369.
  24. H. Cui, X. Yang, Q. Gao, H. Liu, Y. Li, H. Tang, R. Zhang, J. Qin and X. Yan, Facile synthesis of graphene oxide-enwrapped Ag<sub>3</sub>PO<sub>4</sub> composites with highly efficient visible light photocatalytic performance, *Materials Letters*, 2013, **93**, 28-31.
  25. V. Bellat, R. Chassagnon, O. Heintz, L. Saviot, D. Vandroux and N. Millot, A multi-step mechanism and integrity of titanate nanoribbons, *Dalton Transactions*, 2015.
  26. N. Wu, J. Wang, D. N. Tafen, H. Wang, J.-G. Zheng, J. P. Lewis, X. Liu, S. S. Leonard and A. Manivannan, Shape-enhanced photocatalytic activity of single-crystalline anatase TiO<sub>2</sub> (101) nanobelts, *Journal of the American Chemical Society*, 2010, **132**, 6679-6685.
  27. Z.-Y. Yuan, J.-F. Colomer and B.-L. Su, Titanium oxide nanoribbons, *Chemical physics letters*, 2002, **363**, 362-366.
  28. Y. Wang, G. Du, H. Liu, D. Liu, S. Qin, N. Wang, C. Hu, X. Tao, J. Jiao and J. Wang, Nanostructured Sheets of Ti-O Nanobelts for Gas Sensing and Antibacterial Applications, *Advanced Functional Materials*, 2008, **18**, 1131-1137.
  29. R. Hernandez-Delgadillo, D. Velasco-Arias, D. Diaz, K. Arevalo-Niño, M. Garza-Enriquez, M. A. De la Garza-Ramos and C. Cabral-Romero, Zerovalent bismuth nanoparticles inhibit *Streptococcus mutans* growth and formation of biofilm, *International journal of nanomedicine*, 2012, **7**, 2109.
  30. R. Hernandez-Delgadillo, D. Velasco-Arias, J. J. Martinez-Sanmiguel, D. Diaz, I. Zumeta-Dube, K. Arevalo-Niño and C. Cabral-Romero, Bismuth oxide aqueous colloidal nanoparticles inhibit *Candida albicans* growth and biofilm formation, *International journal of nanomedicine*, 2013, **8**, 1645.
  31. A. D. Mani, P. M. K. Reddy, M. Srinivaas, P. Ghosal, N. Xanthopoulos and C. Subrahmanyam, Facile synthesis of efficient visible active C-doped TiO<sub>2</sub> nanomaterials with high surface area for the simultaneous removal of phenol and Cr (VI), *Materials Research Bulletin*, 2015, **61**, 391-399.

32. F. M. Hossain, L. Sheppard, J. Nowotny and G. E. Murch, Optical properties of anatase and rutile titanium dioxide: *Ab initio* calculations for pure and anion-doped material, *Journal of Physics and Chemistry of Solids*, 2008, **69**, 1820-1828.
33. S. B. Rawal, S. D. Sung and W. I. Lee, Novel Ag<sub>3</sub>PO<sub>4</sub>/TiO<sub>2</sub> composites for efficient decomposition of gaseous 2-propanol under visible-light irradiation, *Catalysis Communications*, 2012, **17**, 131-135.
34. R. Liu, P. Hu and S. Chen, Photocatalytic activity of Ag<sub>3</sub>PO<sub>4</sub> nanoparticle/TiO<sub>2</sub> nanobelt heterostructures, *Applied Surface Science*, 2012, **258**, 9805-9809.
35. W. Zhou, G. Du, P. Hu, G. Li, D. Wang, H. Liu, J. Wang, R. I. Boughton, D. Liu and H. Jiang, Nanoheterostructures on TiO<sub>2</sub> nanobelts achieved by acid hydrothermal method with enhanced photocatalytic and gas sensitive performance, *Journal of Materials Chemistry*, 2011, **21**, 7937-7945.
36. W. Teng, X. Li, Q. Zhao, J. Zhao and D. Zhang, *In situ* capture of active species and oxidation mechanism of RhB and MB dyes over sunlight-driven Ag/Ag<sub>3</sub>PO<sub>4</sub> plasmonic nanocatalyst, *Applied Catalysis B: Environmental*, 2012, **125**, 538-545.
37. Y. Lei, L.-D. Zhang, G.-W. Meng, G.-H. Li, X. Zhang, C. Liang, W. Chen and S. Wang, Preparation and photoluminescence of highly ordered TiO<sub>2</sub> nanowire arrays, *Applied Physics Letters*, 2001, **78**, 1125-1127.
38. J. Liu, X. Fu, S. Chen and Y. Zhu, Electronic structure and optical properties of Ag<sub>3</sub>PO<sub>4</sub> photocatalyst calculated by hybrid density functional method, *Applied Physics Letters*, 2011, **99**, 191903.
39. X. Ma, B. Lu, D. Li, R. Shi, C. Pan and Y. Zhu, Origin of photocatalytic activation of silver orthophosphate from first-principles, *The Journal of Physical Chemistry C*, 2011, **115**, 4680-4687.
40. B. Xin, L. Jing, Z. Ren, B. Wang and H. Fu, Effects of simultaneously doped and deposited Ag on the photocatalytic activity and surface states of TiO<sub>2</sub>, *The Journal of Physical Chemistry B*, 2005, **109**, 2805-2809.
41. J. Kiwi and V. Nadtochenko, Evidence for the mechanism of photocatalytic degradation of the bacterial wall membrane at the TiO<sub>2</sub> interface by ATR-FTIR and laser kinetic spectroscopy, *Langmuir*, 2005, **21**, 4631-4641.

42. S. Sontakke, C. Mohan, J. Modak and G. Madras, Visible light photocatalytic inactivation of *Escherichia coli* with combustion synthesized  $\text{TiO}_2$ , *Chemical Engineering Journal*, 2012, **189**, 101-107.
43. G. Gogniat and S. Dukan,  $\text{TiO}_2$  photocatalysis causes DNA damage via Fenton reaction-generated hydroxyl radicals during the recovery period, *Applied and environmental microbiology*, 2007, **73**, 7740-7743.
44. Q. Li, S. Mahendra, D. Y. Lyon, L. Brunet, M. V. Liga, D. Li and P. J. Alvarez, Antimicrobial nanomaterials for water disinfection and microbial control: potential applications and implications, *Water research*, 2008, **42**, 4591-4602.
45. G. A. Sotiriou and S. E. Pratsinis, Antibacterial activity of nanosilver ions and particles, *Environmental science & technology*, 2010, **44**, 5649-5654.
46. M. Rai, A. Yadav and A. Gade, Silver nanoparticles as a new generation of antimicrobials, *Biotechnology advances*, 2009, **27**, 76-83.
47. A. Wu, C. Tian, W. Chang, Y. Hong, Q. Zhang, Y. Qu and H. Fu, Morphology-controlled synthesis of  $\text{Ag}_3\text{PO}_4$  nano/microcrystals and their antibacterial properties, *Materials Research Bulletin*, 2013, **48**, 3043-3048.
48. X. Yang, J. Qin, Y. Jiang, R. Li, Y. Li and H. Tang, Bifunctional  $\text{TiO}_2/\text{Ag}_3\text{PO}_4/\text{graphene}$  composites with superior visible light photocatalytic performance and synergistic inactivation of bacteria, *RSC Advances*, 2014, **4**, 18627-18636.
49. R. Sapkal, S. Shinde, T. Waghmode, S. Govindwar, K. Rajpure and C. Bhosale, Photo-corrosion inhibition and photoactivity enhancement with tailored zinc oxide thin films, *Journal of Photochemistry and Photobiology B: Biology*, 2012, **110**, 15-21.
50. S. Yan, Z. Li and Z. Zou, Photodegradation of rhodamine B and methyl orange over boron-doped  $\text{g-C}_3\text{N}_4$  under visible light irradiation, *Langmuir*, 2010, **26**, 3894-3901.
51. D. Wang, Y. Duan, Q. Luo, X. Li, J. An, L. Bao and L. Shi, Novel preparation method for a new visible light photocatalyst: mesoporous  $\text{TiO}_2$  supported  $\text{Ag}/\text{AgBr}$ , *Journal of Materials Chemistry*, 2012, **22**, 4847-4854.
52. W. Li, D. Li, S. Meng, W. Chen, X. Fu and Y. Shao, Novel Approach To Enhance Photosensitized Degradation of Rhodamine B under Visible Light Irradiation by the  $\text{Zn}_x\text{Cd}_{1-x}\text{S}/\text{TiO}_2$  Nanocomposites, *Environmental science & technology*, 2011, **45**, 2987-2993.

**Figure captions and tables:**

Figure 1. **(a)** X-ray diffraction pattern of combustion synthesized  $\text{TiO}_2$  and acid etched  $\text{TiO}_2$  nanobelts **(b)** X-ray diffraction pattern of  $\text{Ag}_3\text{PO}_4$  and  $\text{Ag}_3\text{PO}_4$  coupled with acid etched  $\text{TiO}_2$  nanobelts.

Figure 2. Diffuse reflectance spectra of  $\text{Ag}_3\text{PO}_4$ , CSTNB and  $\text{Ag}_3\text{PO}_4/\text{CSTNB}$ .

Figure 3. Scanning electron microscopic images of **(a)** pristine nanobelts **(b)** acid etched  $\text{TiO}_2$  nanobelts **(c)**  $\text{Ag}_3\text{PO}_4$  **(d)**  $\text{Ag}_3\text{PO}_4/\text{acid etched TiO}_2$  nanobelt composite, bright field TEM image of **(e)**  $\text{Ag}_3\text{PO}_4/\text{acid etched TiO}_2$  nanobelt composite and HRTEM image of **(f)**  $\text{Ag}_3\text{PO}_4/\text{acid etched TiO}_2$  nanobelt composite.

Figure 4. XPS spectra of Ag in  $\text{Ag}_3\text{PO}_4/\text{CSTNB}$  **(a)** before the reaction **(b)** after the reaction.

Figure 5. Photoluminescence spectra of  $\text{Ag}_3\text{PO}_4/\text{CST}$  and  $\text{Ag}_3\text{PO}_4/\text{CSTNB}$  (inset peak positions).

Figure 6. **(a) & (b)** Photocatalytic degradation and rate kinetics **(c) & (d)** of 20 ppm methylene blue and 30 ppm of methyl orange by  $\text{Ag}_3\text{PO}_4$ ,  $\text{Ag}_3\text{PO}_4/\text{P-25}$ ,  $\text{Ag}_3\text{PO}_4/\text{CST}$  and  $\text{Ag}_3\text{PO}_4/\text{CSTNB}$  under solar irradiation.

Figure 7. Antimicrobial activity of  $\text{Ag}_3\text{PO}_4$ ,  $\text{Ag}_3\text{PO}_4/\text{P-25}$ ,  $\text{Ag}_3\text{PO}_4/\text{CST}$  and  $\text{Ag}_3\text{PO}_4/\text{CSTNB}$  under **(a)** dark conditions **(b)** under solar irradiation.

Figure 8. Evaluation of reactive radical species using various scavengers.

Figure 9. Reusability of **(a)**  $\text{Ag}_3\text{PO}_4$  and **(b)**  $\text{Ag}_3\text{PO}_4/\text{TiO}_2$  nanobelts against methylene blue degradation.

Table 1. Rate parameters for photodegradation of methylene blue and methyl orange by  $\text{Ag}_3\text{PO}_4$ ,  $\text{Ag}_3\text{PO}_4/\text{P-25}$ ,  $\text{Ag}_3\text{PO}_4/\text{CST}$  and  $\text{Ag}_3\text{PO}_4/\text{CSTNB}$  under solar irradiation.

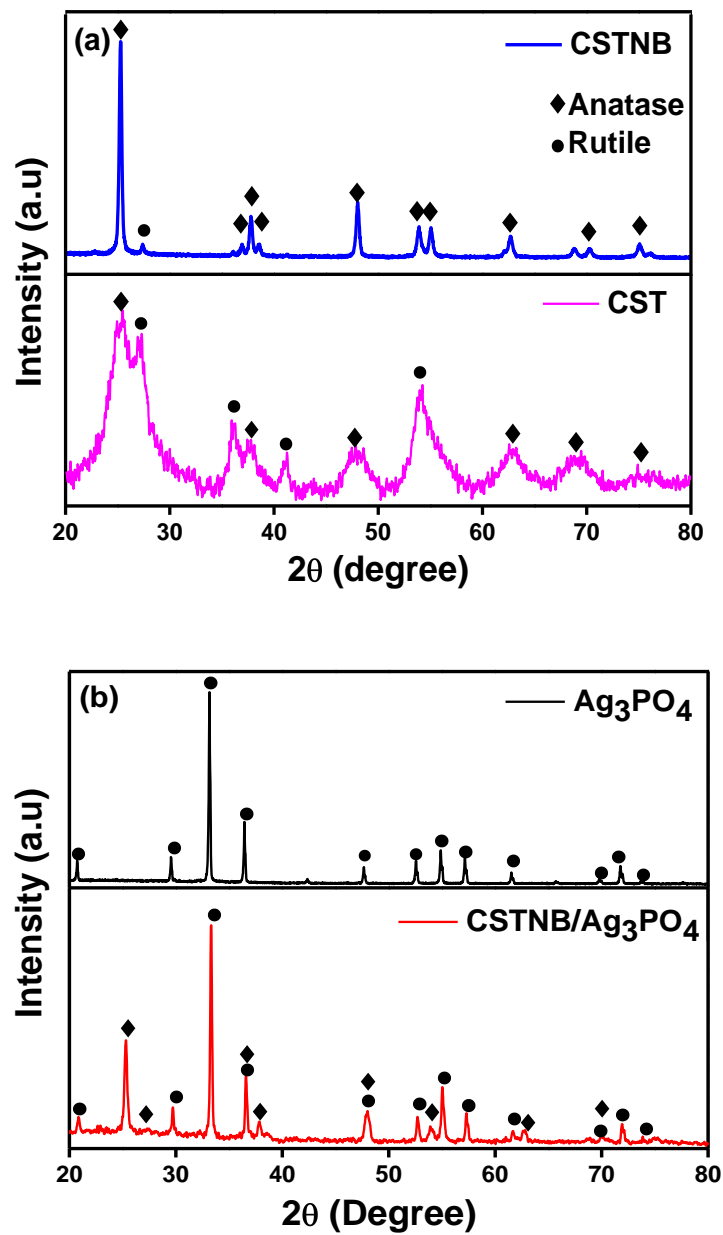


Figure 1. (a) X-ray diffraction pattern of combustion synthesized TiO<sub>2</sub> and acid etched TiO<sub>2</sub> nanobelts  
(b) X-ray diffraction pattern of Ag<sub>3</sub>PO<sub>4</sub> and Ag<sub>3</sub>PO<sub>4</sub> coupled with acid etched TiO<sub>2</sub> nanobelts.



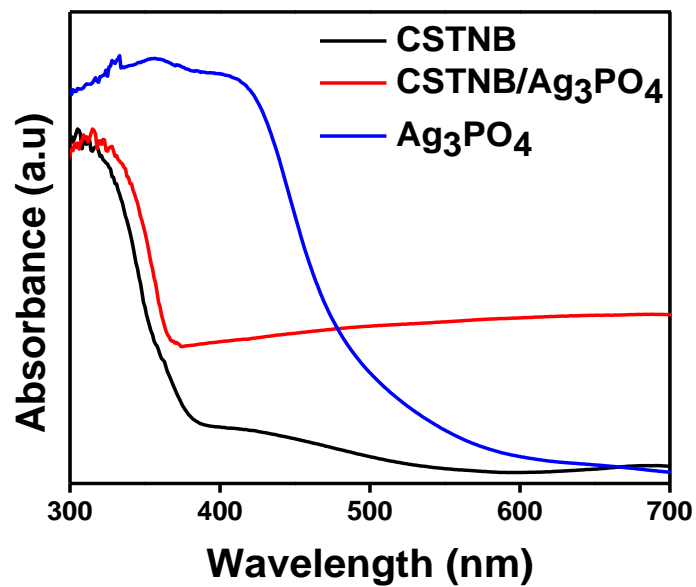


Figure 2. Diffuse reflectance spectra of Ag<sub>3</sub>PO<sub>4</sub>, CSTNB and Ag<sub>3</sub>PO<sub>4</sub>/CSTNB.

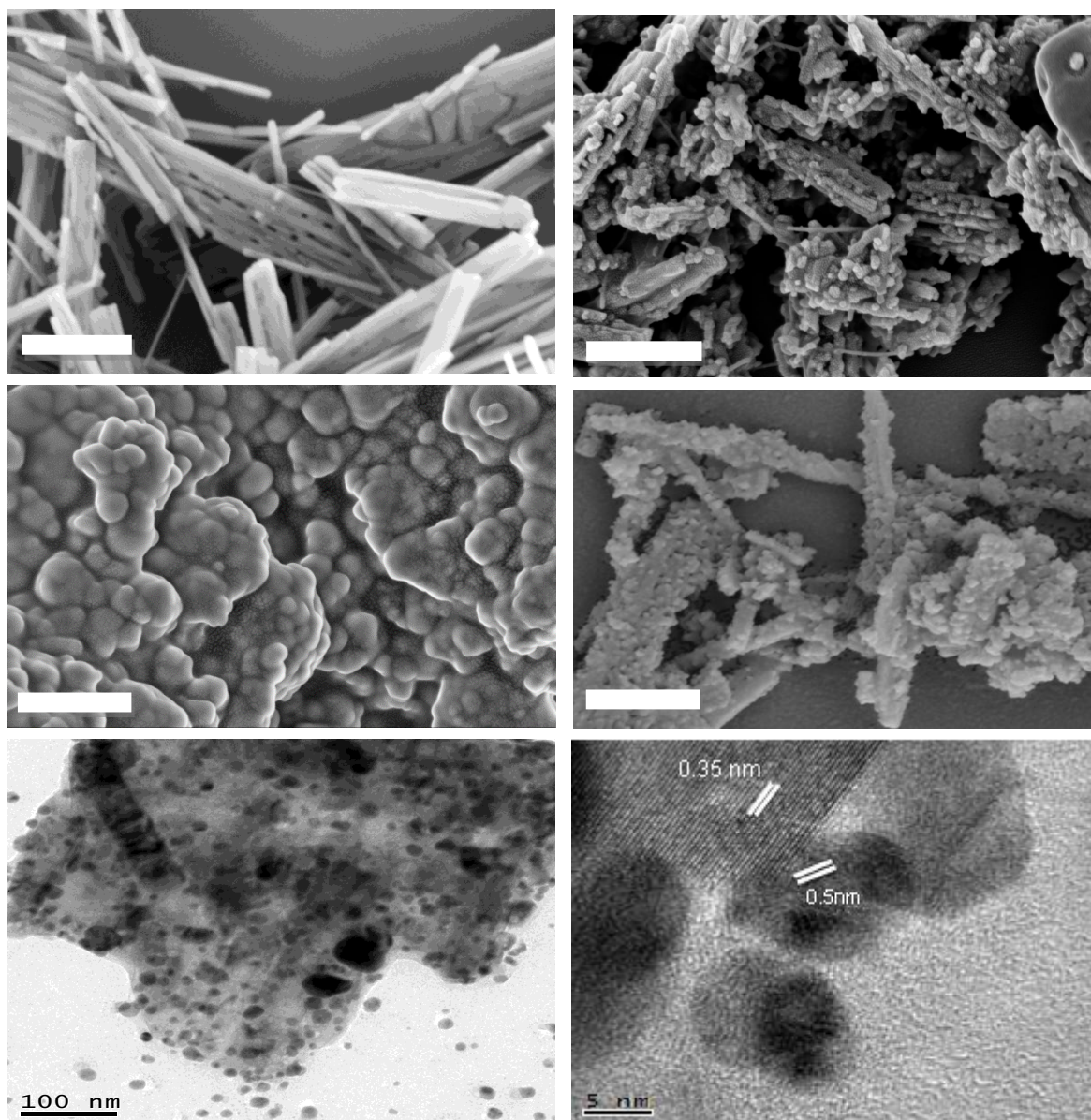


Figure 3. Scanning electron microscopic images of (a) pristine nanobelts (b) acid etched TiO<sub>2</sub> nanobelts (c) Ag<sub>3</sub>PO<sub>4</sub> (d) Ag<sub>3</sub>PO<sub>4</sub>/acid etched TiO<sub>2</sub> nanobelt composite, (e) bright field TEM image of Ag<sub>3</sub>PO<sub>4</sub>/acid etched TiO<sub>2</sub> nanobelt composite and HRTEM image of (f) Ag<sub>3</sub>PO<sub>4</sub>/acid etched TiO<sub>2</sub> nanobelt composite.

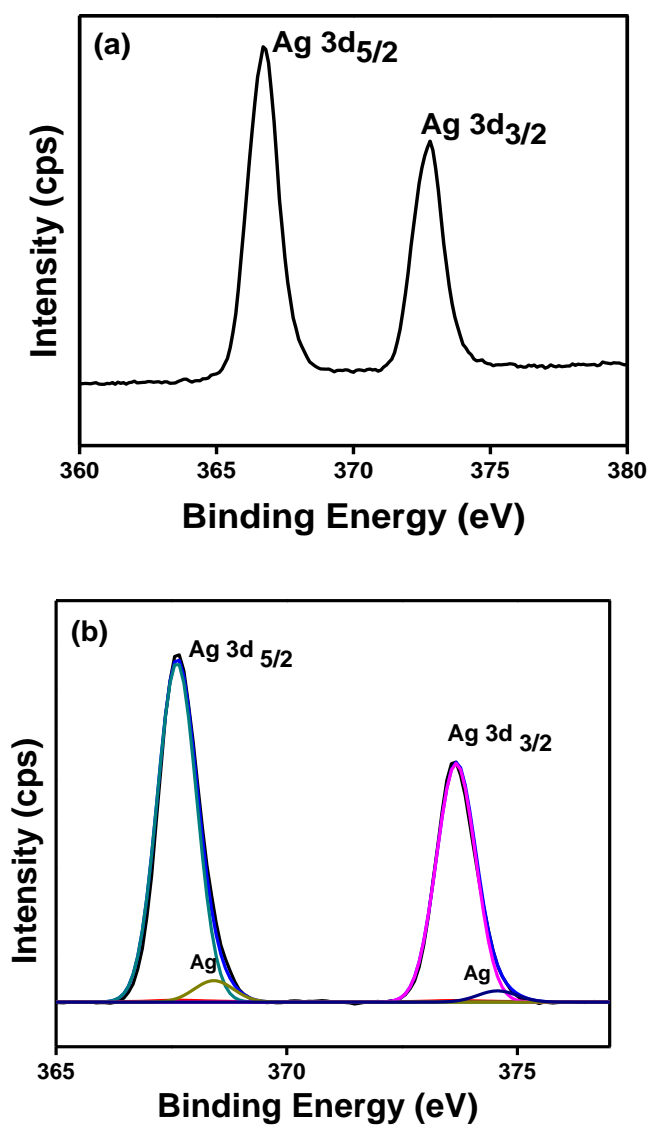


Figure 4. XPS spectra of Ag in Ag<sub>3</sub>PO<sub>4</sub>/CSTNB before the reaction (a) after the reaction.

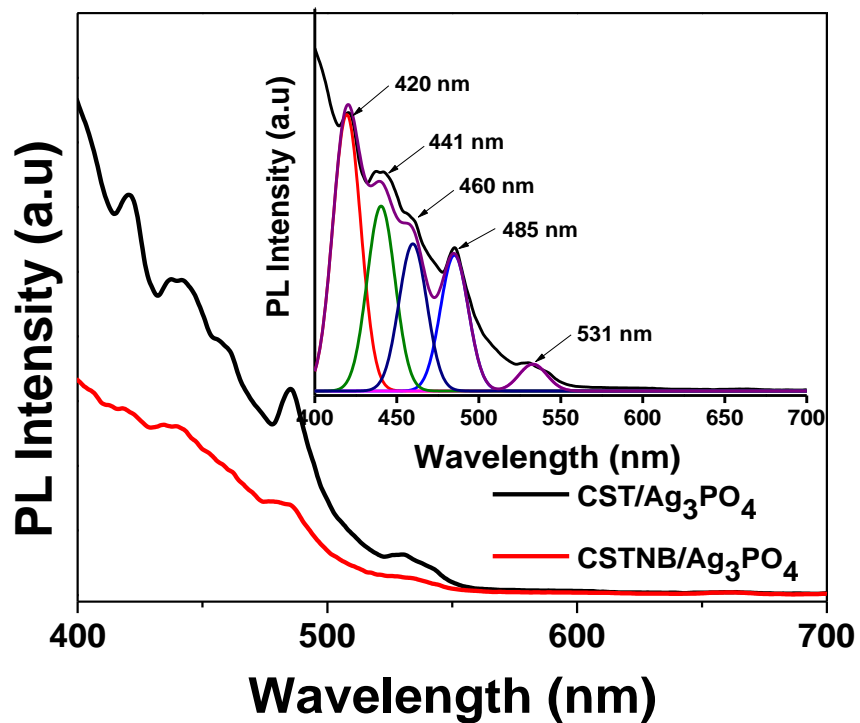


Figure 5: Photoluminescence spectra of CST/Ag<sub>3</sub>PO<sub>4</sub> and CSTNB/Ag<sub>3</sub>PO<sub>4</sub> (inset shows peak positions)

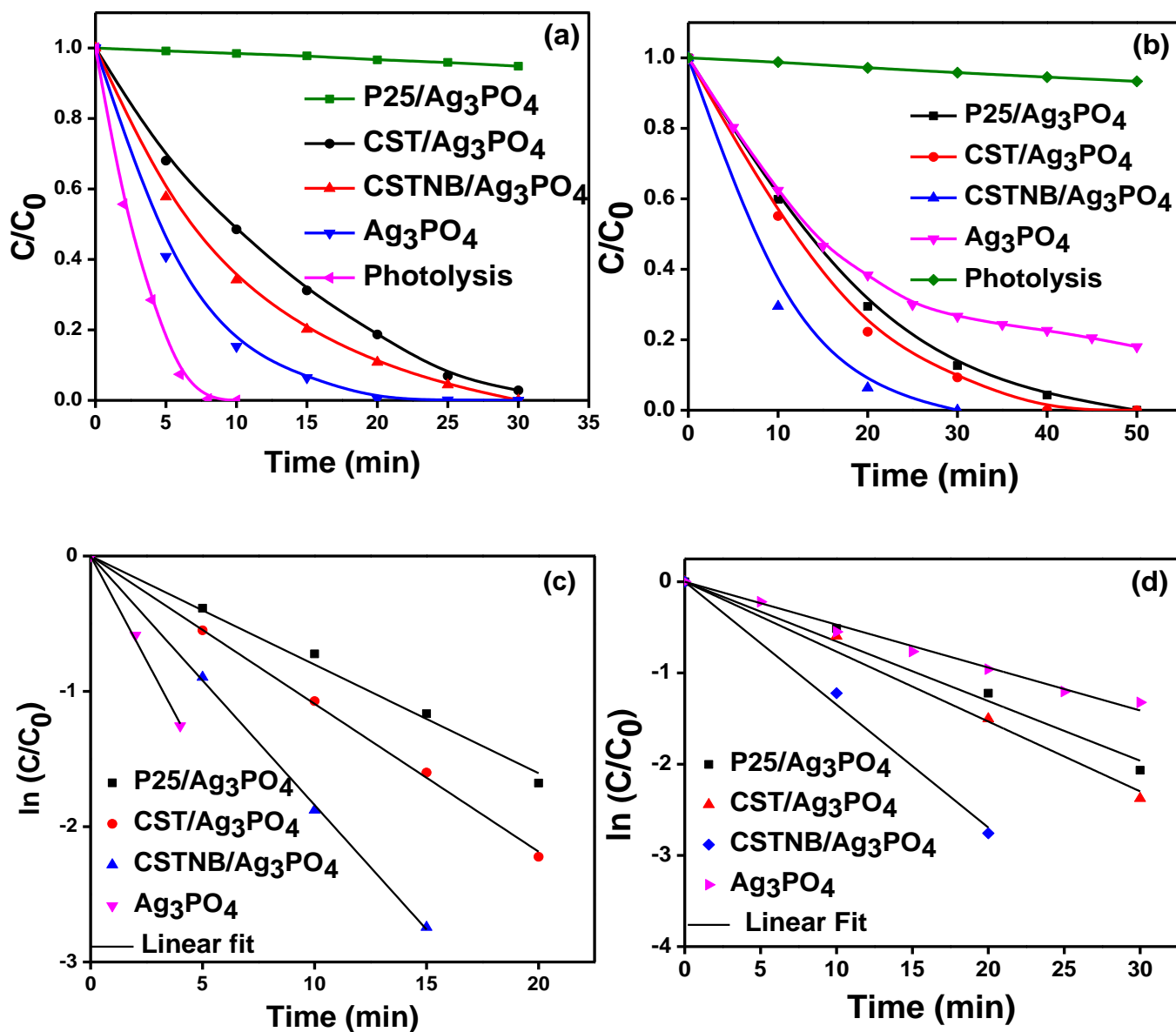


Figure 6. (a) & (b) Photocatalytic degradation and (c) & (d) rate kinetics of 20 ppm methylene blue and 30 ppm of methyl orange by  $\text{Ag}_3\text{PO}_4$ ,  $\text{Ag}_3\text{PO}_4/\text{P-25}$ ,  $\text{Ag}_3\text{PO}_4/\text{CST}$  and  $\text{Ag}_3\text{PO}_4/\text{CSTNB}$  under solar irradiation.

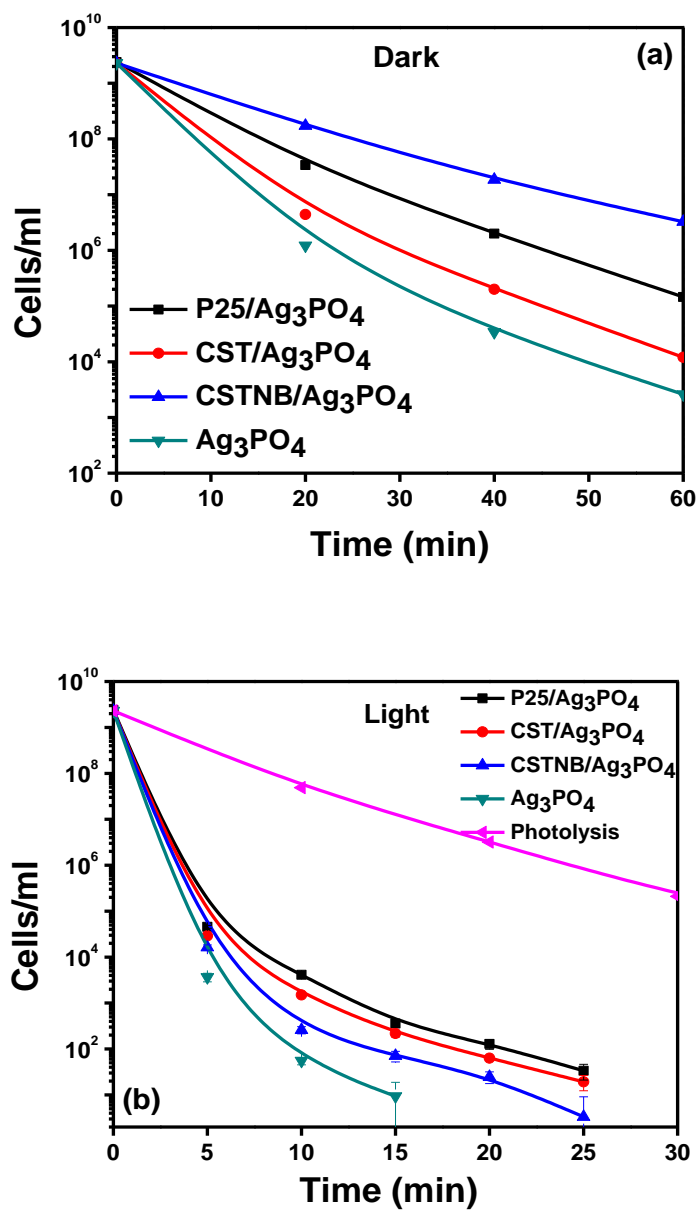


Figure 7. Antimicrobial activity of Ag<sub>3</sub>PO<sub>4</sub>, Ag<sub>3</sub>PO<sub>4</sub>/P-25, Ag<sub>3</sub>PO<sub>4</sub>/CST and Ag<sub>3</sub>PO<sub>4</sub>/CSTNB under (a) dark conditions (b) under solar irradiation.

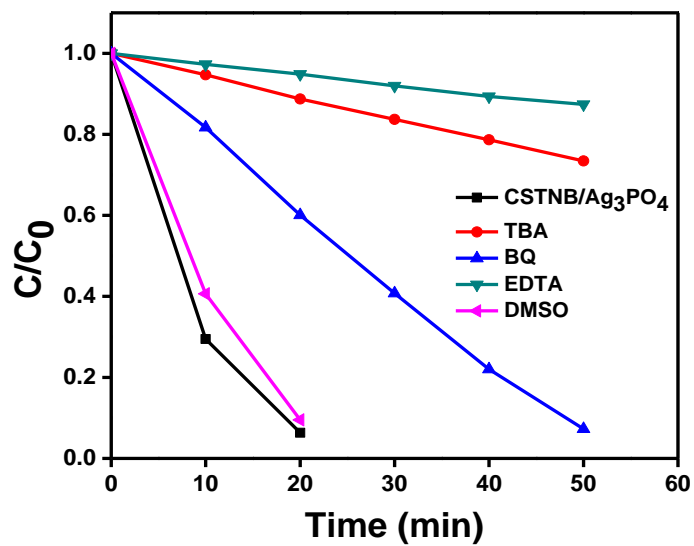


Figure 8. Evaluation of reactive radical species using various scavengers.

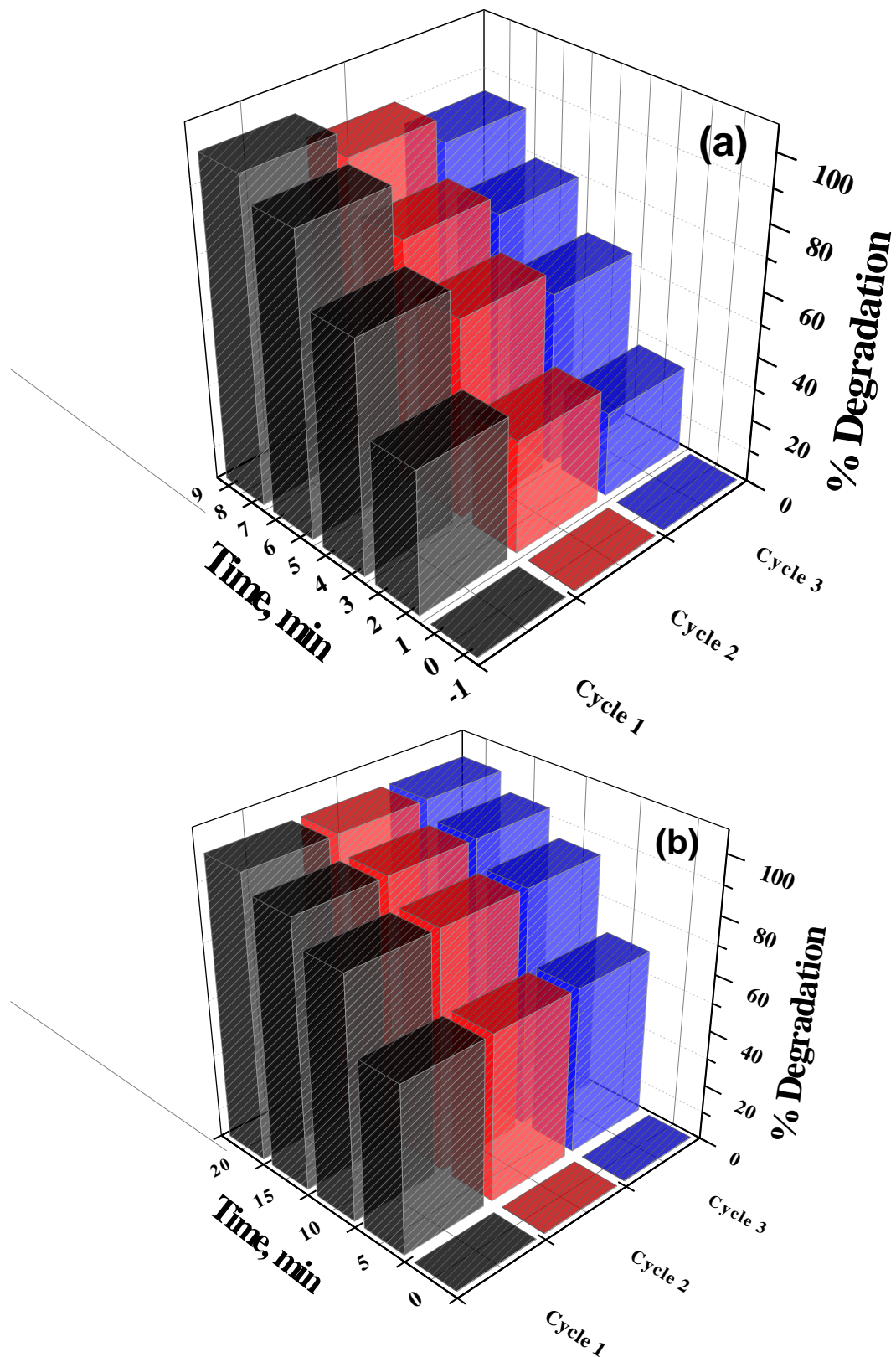


Figure 9. Reusability of (a)  $\text{Ag}_3\text{PO}_4$  and (b)  $\text{Ag}_3\text{PO}_4/\text{TiO}_2$  nanobelts for methylene blue degradation.



Catalyst	Rate constant, k ( $\times 10^{-4} \text{min}^{-1}$ )	
	Methylene blue	Methyl Orange
Ag <sub>3</sub> PO <sub>4</sub> /Degussa P-25	802 $\pm$ 2.3	759 $\pm$ 87.9
Ag <sub>3</sub> PO <sub>4</sub> /Combustion synthesized TiO <sub>2</sub>	1092 $\pm$ 2.1	762 $\pm$ 7.2
Ag <sub>3</sub> PO <sub>4</sub> /Acid etched TiO <sub>2</sub> Nanobelts	1840 $\pm$ 3.3	1354 $\pm$ 6.7
Ag <sub>3</sub> PO <sub>4</sub>	3096 $\pm$ 15.3	445 $\pm$ 3.2

Table 1. Rate parameters for photodegradation of methylene blue and methyl orange by Ag<sub>3</sub>PO<sub>4</sub>, Ag<sub>3</sub>PO<sub>4</sub>/P-25, Ag<sub>3</sub>PO<sub>4</sub>/CST and Ag<sub>3</sub>PO<sub>4</sub>/CSTNB under solar irradiation.